IOP Publishing Measurement Science and Technology
Meas. Sci. Technol. **31** (2020) 054004 (16pp) https://doi.org/10.1088/1361-6501/ab6672

Application of 3D-PTV to mass exchange in an open-channel flow past a lateral embayment

L Engelen and T De Mulder

Hydraulics Laboratory, Dept. of Civil Engineering, Ghent University, Sint-Pietersnieuwstraat 41 B5, B-9000 Ghent, Belgium

E-mail: Lukas.Engelen@UGent.be

Received 8 October 2019, revised 10 December 2019
Accepted for publication 31 December 2019
Published 6 February 2020

Abstract

This work presents the design and application of a Lagrangian measurement and analysis methodology, which is employed to study the flow and passive tracer exchange between a main channel and a lateral cavity in a laboratory experiment. For this purpose, a 3D-PTV system is implemented for which a static and dynamic experimental validation show that the use of a multiplane camera calibration technique and a recent trajectory linking strategy allow one to track the neutrally buoyant particles accurately in time. The resulting 3D particle trajectories are then used to quantify the 3D flow field and study the entrainment mechanisms between the main flow and the cavity using an Eulerian and a Lagrangian methodology, respectively. Analysis of the flow velocities at the geometrical interface between the main flow and the cavity indicates that the inflow is mainly concentrated at the downstream end of the cavity opening, closer to the bottom, while the particles tend to leave the cavity in the upstream part of the interface more uniform over the water depth. A vertical profile of the mass exchange coefficient is quantified based on the transverse velocity components at the interface, which confirms that the exchange intensity varies significantly with depth. More importantly, however, a novel Lagrangian trajectory classification strategy is proposed to study the transport of particles more in detail and overcome problems related to the time-dependent and 3D shape of the hydrodynamic boundary between the main channel and the cavity. Compared to the common Eulerian approach, this enables to refine the definition of mass exchange and exclude those particles that do not add to the net exchange. Subsequently a Lagrangian definition of the (depth-averaged) mass exchange coefficient is proposed, for which the current (preliminary) results indicate its potential to reliably quantify mass exchange.

Keywords: 3D-PTV, lateral cavity, mass exchange, passive tracer transport, Lagrangian analysis

(Some figures may appear in colour only in the online journal)

1. Introduction

Open-channel flow past a lateral, semi-enclosed basin, also referred to as a cavity, a lateral embayment or a dead-zone, is encountered in various hydrodynamic situations, such as the (river or coastal) flow past a natural embayment, a harbor, a dock, an access channel to a navigation lock, groyne fields, etc. For both economic and ecological reasons, it is important to understand the global flow field within the cavity and the exchange processes (of e.g. nutrients, pollutants, sediments) between the (river or coastal) current and this lateral embayment. Research on lateral cavities often studies basins with a simplified planform geometry, like e.g. a rectangular or, as in the present case, square shape. For the latter, previous research

 © 2020 IOP Publishing Ltd Printed in the UK

(e.g. Mignot *et al* 2019) showed that a single main gyre occupies almost the whole of the cavity area, in addition to corner structures that are generated by vortex-wall interactions.

Both experimental and numerical work has been done to study the influence of dead zones on the transport processes in riverine environments. Given the large spatial extent of the entire river system, the modeling of mass and/or passive tracer transport was mainly restricted to 1D approaches (Taylor 1954, Hays 1966) to estimate the longitudinal dispersion of a passive tracer cloud. Similarly to Taylor (1954), Valentine and Wood (1979) modelled the mass entrainment in the dead zone as a first order system using a non-dimensional entrainment coefficient k. Based on experimental results, they suggested a constant value $k = 0.02 \pm 0.01$, independent of the dead zone geometry.

Numerous research studies on mass exchange have focused on the influence of the dead zone geometry and the flow conditions on the exchange by quantifying this mass exchange coefficient k (e.g. Uijttewaal *et al* 2001, Weitbrecht *et al* 2008, Mignot *et al* 2017). Experimentally, k is usually determined by one of two possible approaches. The 'transverse velocity method' estimates k by integration of the measured transverse velocities along the main channel-cavity interface, whereas the 'dye release method' quantifies k from the time evolution of the depth-averaged dye concentration inside the cavity. However, previous research has shown that the scatter of the estimated k values using the same approach (different flow configurations) and between the two methodologies (same flow configuration) is significant. In this work, we investigate more in depth the simplifications made by the transverse velocity method, and the resulting limitations to describe mass exchange.

As a first simplification, most experimental studies quantify k by integration (along a horizontal transect of the interface) of the transverse velocities measured in a single horizontal plane, either at the free surface (using surface particle tracking) or at a depth that is considered representative for the depth-averaged flow field (using sub-surface particle image velocimetry). Even though the flow field within the cavity is quasi-uniform over the water depth, Tuna *et al* (2013) and Akutina (2015) showed that, especially near the geometrical interface, the flow patterns just above the bed deviated significantly. The inflow from the main stream to the cavity was found to be concentrated in the downstream part of the interface and primarily near the bed. After being transported inside the cavity by the secondary recirculation (Mizumura and Yamasaka 2002, Jamieson and Gaskin 2007), outflow from the cavity towards the main stream occurred mainly in the upstream part of the interface and closer to the surface. Moreover, the distribution of vortical flow features, which are of major importance for the fluid and mass exchange, seemed highly dependent on depth, thus indicating their 3D character. Therefore, a 2D approach seems questionable to reliably describe the mass exchange with a lateral embayment.

Quantitative evidence of this failure of the 2D flow approximation was first shown by Uijttewaal *et al* (2001), in which the k values determined using the transverse surface velocities differed by almost a factor of 2 from the k values based on the depth-averaged dye concentration. The error made by a 2D simplification was confirmed by comparison of depth-averaged large eddy simulations (LES) and 3D LES of a shallow embayment (e.g. Hinterberger *et al* 2007, Constantinescu *et al* 2009), in which the depth-averaged LES results strongly overpredicted the mass exchange. Moreover, using the transverse velocity method, Tuna *et al* (2013) and Akutina (2015) measured the vertical profile of the mass exchange coefficient and showed that it varied up to 25% as compared to its depth-averaged value.

The second simplification, which will be described more in detail later in this paper, is that all transverse velocity fluctuations at the interface are integrated, even though they do not necessarily contribute to the net fluid or mass exchange, as pointed out by Prof. Uijttewaal in Akutina (2015).

To better understand how mass is transported in and out of a lateral embayment, state-of-the-art measurement techniques are needed that are able to capture the 3D aspect of the exchange. In the past few years, 3D particle tracking velocimetry (3D-PTV) has gained popularity compared to (planar) PIV or Acoustic Doppler Velocimetry because of several advantages: non-intrusive, high 3D spatial resolution, Lagrangian trajectory information, etc.

Therefore, the first part of this paper describes the design, validation and application of a recent 3D-PTV setup. In particular, we emphasize several key aspects that are crucial for reliable and accurate 3D results and present a detailed description of the adopted methodologies for calibration, validation and post-processing of the 3D-PTV technique. The 3D-PTV (laboratory) setup is applied to study the flow and mass exchange in a (square) cavity flow by means of passive and neutrally buoyant tracer particles. Note that the behavior of the latter is not necessarily representative for all types of mass exchange (e.g. sediment). The resulting particle trajectories are then used to quantify the 3D flow field and the common Eulerian mass exchange coefficient.

The second part of this work presents a novel Lagrangian definition of the mass exhange coefficient based on the individual particle trajectories. With the aim of identifyiying the particles that contribute to the actual net exchange, we present a trajectory classification system that avoids ambiguities related to the time-dependent and 3D shape of the hydrodynamic boundary between the main channel and the cavity. Subsquently, the presented Lagrangian definition of k is tested on the current dataset to illustrate the added value of the presented methodology.

2. Cavity facility

The experiment described in this work are conducted in the Hydraulics Laboratory of Ghent University, Belgium. The cavity facility (figure 1) consists of a polycarbonate-walled flume with a total length of 2.5 m and a rectangular cross-section with a width b of 0.08 m. The main channel is connected to a square side embayment, having a length L and width W of 0.08 m (figure 1), with the upstream corner of the cavity located at 2 m downstream from the inlet of the flume. At this

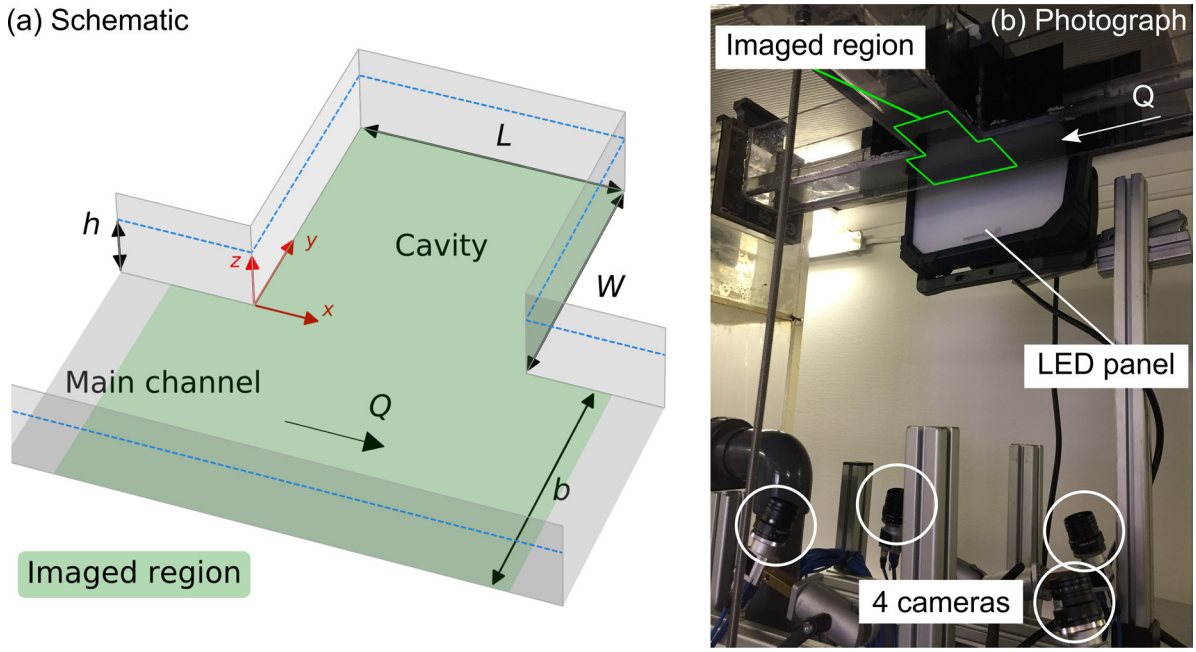

Figure 1. Schematic (a) and photograph (b) of the experimental setup, with the (square) cavity dimensions L and W equal to the width b of the main channel (0.08 m) and the water depth h equal to 27 mm, hence $h/L \approx 0.34$. The adopted coordinate system in this work is drawn in red, while the overlapping field of view of the four cameras (mounted below the flume) is indicated in green.

inlet of the main channel, a honeycomb mesh is installed to stabilize and straighten the inflow, while a floating body is used to suppress surface irregularities due to the honeycomb.

For the present experiment, the bed is horizontal with an average water depth h of 27 mm, hence $h/L \approx 0.34$. The inlet discharge is fixed to $Q = 0.34$ l s^{-1} and measured using an electromagnetic flowmeter (accuracy of $\pm$ 0.003 l s^{-1}) within the pumping loop. The average bulk velocity in the main channel thus equals $U_b = Q/bh = 0.16$ m s^{-1}, giving a subcritical Froude number of $\mathrm{Fr} = U_b/\sqrt{gh} = 0.31$ (similar to flow configurations of e.g. Tuna *et al* 2013, Akutina 2015). The Reynolds number of the main stream equals $\mathrm{Re} = \frac{4\rho_f U_b bh}{\mu_f(b+2h)} \approx 1.00 \times 10^4$, with ρ_f and μ_f the density and dynamic viscosity of the fluid (water). Since salt is added to the water to approach the material density of the seeding particles (see section 3.2), Re was computed with a density $\rho_f = 1050$ kg m^{-3} and $\mu_f = 1.067 \times 10^{-3}$ kg m^{-1} s^{-1} for an average water temperature of 24 °C.

3. Three-dimensional particle tracking velocimetry (3D-PTV)

Three-dimensional particle tracking velocimetry (3D-PTV) is a Lagrangian flow measurement technique to determine flow velocities within a 3D observation volume. The technique relies on flow visualization using small and usually neutrally buoyant particles. By recording the particles from different viewing angles, their 3D coordinates can be determined using spatial and temporal stereoscopic correspondence matching, for which in this work the epipolar line intersection technique is used (e.g. Maas *et al* 1993). In the following, the design of the different components of the presented 3D-PTV setup are described more in detail.

3.1. Optical set-up

Reconstruction of the individual 3D positions of the detected particles relies on stereoscopic matching between the different camera views. Since individual particles cannot be distinguished from each other based on distinctive particle features (e.g. size, shape, or color), only the fact that the 'lines of sight' from different cameras need to pass through the particle center can be used. To that end, two cameras are theoretically sufficient to solve the 3D reconstruction problem. However, ambiguities in stereoscopic correspondences can arise if two or more particle images are found in the same search area of the correspondence matching algorithm. Such ambiguities can be minimized by limiting the seeding density, increasing the number of cameras, optimizing the camera arrangement and ensuring accurate camera calibration.

With regard to the optimal camera arrangement, Dracos (2013) showed that for a reasonable particle seeding density and optical setup, at least three cameras are needed to guarantee reliable 3D positions. Maas *et al* (1993) reduced the number of ambiguities in the epipolar matching algorithm by at least one order of magnitude by using three instead of two cameras. By adding a fourth camera, the remaining ambiguities diminished to almost zero and allowed a reliable 3D particle position even in case particles were hidden in one of the four images. Moreover, the accuracy of the reconstructed coordinates improved with a factor of 1.3 and 1.7 for a three and four camera setup, respectively.

Given the superior performance of four independent camera views, the current optical setup (figure 1) comprises four monochrome CMOS sensor cameras (Basler Ace, 10 Bit, 1920 × 1200 pixels) mounted below the flume in a square arrangement as suggested by Maas *et al* (1993). Compared to 3D-PTV with cameras installed above the free surface

(Akutina *et al* 2018), the constant refraction through the flat bottom of the flume can more easily be corrected for. The camera recordings are synchronized by an external pulse generator (NI 6601) at a frame rate of 150 Hz and a shutter speed of 1/500 s, while a total measurement period of 120 s proved sufficient for convergence of the time-averaged velocities.

In combination with the camera lens, the distance between the cameras and the observed measurement volume is an important design parameter. It affects the total volume that is observed by all four cameras, but also determines the size of the projection of a seeding particle on the cameras' CCD (in pixels) and the cameras' depth of field. As a compromise between these conflicting design considerations, the average vertical distance between the cameras and the bottom of the flume is chosen around 530 mm, with the angle between the optical axes of the cameras $\cong 40°$ as suggested by Kieft *et al* (2002) and Walpot *et al* (2006). The cameras are fitted with lenses having a fixed focal distance of 35 mm, being a trade-off between a large depth of field and a large field of view. Figure 1(b) shows the installed cameras, each capturing the entire cavity and adjacent main channel region with an average magnification of ≈ 11 pixels mm^{-1}. During the recording period, the observation domain is lighted from the side by a high-lumen LED panel as a cost-effective solution compared to advanced and specialized light sources. Additional precautions are taken to minimize reflections of the water surface and avoid a non-uniform background when viewing the lighted volume from below.

3.2. Particle seeding

The flow is seeded with small polystyrene microspheres with a density of $\rho_p = 1060$ kg m^{-3} and a particle diameter d_p of $212 - 250\,\mu$m, in which a continuous recirculation and mixing in the upstream tank ensures an approximately constant supply of particles through the main channel. The particle size in the images equals 2–3 pixels, which is sufficiently large ($\geqslant 2$ pixels) to avoid peak-locking (Adrian and Westerweel 2011, Raffel *et al* 2018). Based on Marxen *et al* (2000), the expected localization accuracy using a Gaussian centroid operator (see section 3.4) for particles of 2–3 pixels is in the order of 0.1 pixel, corresponding to a horizontal distance of 0.09 mm in the imaged region. To minimize inertial effects and make the particles as neutrally buoyant as possible, salt is added to the water to increase the water density to approximately $\rho_f = 1050$ kg m^{-3}. This reduces the amount of particles settling in low-velocity regions of the cavity, while avoiding that particles tend to float on the water surface.

The importance of the finite-size of the particles can be estimated by comparing the time scale of the flow fluctuations with the particle relaxation time, usually expressed as the Stokes number $\mathrm{St} = \tau_p/\tau_f$. The Kolmogorov time scale is used as a representative fluid time scale $\tau_f = (\nu_f/\epsilon)^{1/2}$ in which ν_f equals the kinematic viscosity of the salt water at 24 °C ($\nu_f = 1.017 \times 10^{-6}$ m^2 s^{-1}) and ϵ is the turbulent dissipation rate of the flow. According to Taylor (1935), the latter can be estimated as $\epsilon = u_{rms}^3/\mathcal{L}$, with u_{rms} the root mean square velocity of the flow fluctuations (estimated as $0.15\,U_b$, based on Mignot *et al* 2016) and $\mathcal{L}$ the integral length scale, which is chosen equal to the water depth h ($= 0.027$ m). In the limit of vanishing particle Reynolds number, the particle response time is given by $\tau_p = \frac{\rho_p}{\rho_f}\frac{d_p^2}{18\,\nu_f}$. However, because of the non-negligible particle size adopted in the current experiment, this work uses a corrected definition for finite particle Reynolds numbers as presented by Xu and Bodenschatz (2008). This results in a Stokes number $\mathrm{St} = 0.04$, which is well below 0.1 such that the tracing accuracy errors are assumed to be negligible (<1%) (Tropea *et al* 2007).

The selected seeding density is a trade-off between maximizing the number of particles per image and minimizing ambiguities during correspondence matching and/or linking of the particles over the image sequence. For the results presented in sections 5.1 and 5.2, about 500 particles are identified and tracked in every frame. Additional thresholds are set to reduce ambiguities and obtain longer trajectories for the Lagrangian classification of section 5.3, maintaining 350 particles per frame on average.

3.3. Camera calibration

Calibration of the camera setup is of crucial importance for accurate and reliable particle trajectories, and aims to determine both the external (position, orientation) and internal (focal distance, principal point, image distortion) camera parameters. Using a set of 25 images of a planar calibration checkerboard prior to the experiment, the internal camera parameters are for every camera estimated using the multi-view Zhang's camera calibration algorithm implemented in OpenCV (Bradski 2017).

To determine the relationship between the 2D image coordinates and the actual 3D positions of the particles, the most straightforward approach is a typical *in situ* calibration method with a multitude of calibration points. This method estimates the cameras' position and orientation as the result of a least-squares optimization relating the imaged calibration points to their known 3D location with respect to the chosen coordinate system. For accurate 3D calibration, the size of the calibration object should match the size of the measurement volume, with well-contrasted calibration points that are evenly spaced in all three directions.

The most common approach with 3D-PTV practitioners is to use a (3D) volumetric (often ziggurat-shaped) calibration object, of which distinctive target points lay on different depths along the cameras' viewing direction. However, in case the depth of the intended measurement volume (in the viewing direction) is significant, a single solid-body makes it impossible to obtain 3D calibration points that are well-distributed in all three directions. Therefore, this work employs 'the multiplane calibration technique' (Walpot *et al* 2006, Kreizer and Liberzon 2011) using an in-house made calibration unit.

The calibration unit consists of a stiff and black-coated aluminum plate, engraved with a white, rectangular pattern of 14×25 dots (diameter = 0.5 mm) with a spacing of 5 mm, of which the engraving accuracy < 0.01 mm. During calibration,

thus prior to the measurements, the calibration plate is positioned inside the flume such that almost the entire imaged region (figure 1) is covered. Using a toothed rod (vertical) motion system of which one end is rigidly attached to the top side of the calibration plate, the pattern can be accurately moved across the water depth. For this work, five parallel horizontal planes (equally spaced between 5 and 25 mm above the bottom of the flume) are combined to create a virtual 3D calibration object, i.e. a $14 \times 25 \times 5$ grid with a spacing of 5 mm in every direction. At every vertical position of the calibration plate, images are taken while the water level is kept stationary above the measurement volume.

The 2D–3D mapping relationship from camera image space to world coordinates (coordinate system indicated in figure 1) is then determined using OpenPTV (OpenPTV-Consortium 2014) (see further), in which refraction at the bottom of the flume is immediately taken into account following the procedure of Maas *et al* (1993). Herewith, the refractive index of the polycarbonate flume is estimated at 1.6, while a refraction index of 1.35 is used for water at the ambient temperature and salt content. To check the quality of the calibration, the residual calibration error is computed by treating the calibration images as input for the 3D reconstruction algorithm. Averaged over all calibration points, the mean difference between the 3D-PTV reconstructed positions and the known 3D coordinates equals 0.016 mm, 0.026 mm and 0.037 mm in the x-, y-, and z-direction, respectively. Compared to the estimated accuracy of particle localization (0.09 mm), these residual calibration errors seem acceptable.

3.4. Data processing

Prior to the 3D-tracking analysis, the recorded images are undistorted using OpenCV routines (Bradski 2017). To facilitate particle detection and improve the accuracy and reliability of tracking, the images are then further edited using Fiji (Schindelin *et al* 2012) by eliminating background noise and gray level variations due to inhomogeneous illumination intensity. Additionally, a Gaussian image filter ($\sigma = 2$ pixels) is applied to minimize localization inaccuracies of the particles' centers that can arise due to illumination differences caused by particle–particle blocking from the light source.

Reconstruction of the 3D particle trajectories using the improved and undistorted images can be subdivided in three main stages: (i) particle recognition, (ii) establishment of correspondences and (iii) particle tracking. These main steps are done using the open-source software OpenPTV (OpenPTV-Consortium 2014, Meller and Liberzon 2016), which was originally developed by ETH Zürich (Willneff 2003) and is still further being developed by an international team of developers (including the current first author). Particles are detected in each frame with subpixel accuracy by a centroid operator and filtered based on their size and brightness in the image to reduce the amount of erroneous detections. The 3D coordinates of the detected particles are then found by correspondence matching between the different camera views using the method of epipolar lines. Herewith, the 3D coordinates of the particles are searched by optical triangulation, for which the results of the calibration process are used to define the perspective imaging geometry. Once the 3D coordinates are obtained, a predictive linking strategy is employed to track the particles throughout subsequent images in time.

The particle trajectories obtained with OpenPTV are then further analyzed with in-house code to increase the length of short trajectories caused by particle 'dropout', where a tracked particle is not detected for a few number of successive frames and then reappears. In OpenPTV, it is currently not possible to link these 'lost particles' with their subsequent reappearance. However, in case the camera frame rate is sufficiently high compared to the particle velocity, the position of the lost particles in later frames can often roughly be predicted based on extrapolation of their trajectory history.

To that end, this work uses the particle prediction and linking algorithm of Xu (2008), in which particle trajectory segments are linked in a 6D position-velocity space. As an extension of the usual particle-tracking techniques that only link particle positions throughout time, they showed that linking interrupted trajectory segments using both position and velocity consistency improves the tracking-efficiency significantly.

For a trajectory segment i that ends at time t_i^{e}, the particle position $\boldsymbol{x}_i^{\mathrm{p}}$ and velocity $\boldsymbol{u}_i^{\mathrm{p}}$ for the start of a new trajectory at a time $t > t_i^{\mathrm{e}}$ are predicted as

$$\begin{cases} \boldsymbol{x}_i^{\mathrm{p}}(t) = \boldsymbol{x}_i^{\mathrm{e}} + \boldsymbol{u}_i^{\mathrm{e}}(t - t_i^{\mathrm{e}}) \\ \boldsymbol{u}_i^{\mathrm{p}}(t) = \boldsymbol{u}_i^{\mathrm{e}} + w_{\mathrm{a}}\boldsymbol{a}_i^{\mathrm{e}}(t - t_i^{\mathrm{e}}) \end{cases} \tag{1}$$

where $\boldsymbol{x}_i^{\mathrm{e}}, \boldsymbol{u}_i^{\mathrm{e}}$ and $\boldsymbol{a}_i^{\mathrm{e}}$ are the position, velocity and acceleration of the particle at time t_i^{e}. The weighting function w_{a} accounts for the uncertainty and variation of the acceleration over a time period $(t - t_i^{\mathrm{e}})$. Similarly as suggested by Xu (2008), a sensitivity analysis on the influence of w_{a} (not shown in this paper) revealed that the best linking results are found for $w_{\mathrm{a}} = 0$. The latter can be explained by the fact that, as the second derivative of the detected particle positions, particle acceleration is highly sensitive to measured position inaccuracies.

The novel idea of Xu (2008) is to reformulate the linking distance between an earlier segment i and a later segment j in physical–velocity space:

$$d_{ij} = \sqrt{\left\|\boldsymbol{x}_i^{\mathrm{p}}(t_j^{\mathrm{s}}) - \boldsymbol{x}_j^{\mathrm{s}}\right\|^2 + \left[\left\|\boldsymbol{u}_i^{\mathrm{p}}\left(t_j^{\mathrm{s}}\right) - \boldsymbol{u}_j^{\mathrm{s}}\right\|\left(t_j^{\mathrm{s}} - t_i^{\mathrm{e}}\right)\right]^2} \tag{2}$$

where $\|.\|$ denotes the Euclidean distance (L_2 norm), t_j^{s} is the starting time of segment j with starting position $\boldsymbol{x}_j^{\mathrm{s}}$ and starting velocity $\boldsymbol{u}_j^{\mathrm{s}} \cdot \boldsymbol{x}_i^{\mathrm{p}}(t_j^{\mathrm{s}})$ and $\boldsymbol{u}_i^{\mathrm{p}}\left(t_j^{\mathrm{s}}\right)$ are the predicted particle position and velocity following segment i at time t_j^{s} (equation (1)), in which $t_j^{\mathrm{s}} > t_i^{\mathrm{e}}$ is a natural condition for segment i and j to be linked.

Linking broken trajectories is then done by first computing d_{ij} for all trajectories starting within a maximum allowed gap time after t_i^{e}, which is in this work limited to 10 frames $(= 10/(150\,\mathrm{Hz}) = 0.07\,\mathrm{s} \cong 1.5\ \tau_{\mathrm{f}})$. From all these candidate segments $\{1, \ldots, k\}$, the most suitable segment j is then connected to the earlier segment i if:

$$d_{ij} = \min_k (d_{ik}) \leqslant d_{\max} \tag{3}$$

where $d_{\max}$ denotes the maximum allowed linking distance for reliable matching. A suitable value for $d_{\max}$ depends on the amount of filtering that is used after preliminary linking and computation of the positions, velocities and accelerations of the (broken) trajectories. In this work, we apply the least-squares Savitzky–Golay smoothing filter to the trajectories obtained with OpenPTV, in which a third order polynomial in a window of 5 frames proved successful to obtain reliable velocities without significant attenuation of the small scale particle motions. For the present results, $d_{\max}$ is chosen equal to 5 mm, which is less than the average particle distance throughout the measurements ($\approx$ 6 mm).

4. Validation

Possible error sources of 3D-PTV can be grouped based on the multiple stages during 3D trajectory reconstruction: (i) identification of the particles in the images of every camera, (ii) 3D particle reconstruction by epipolar correspondence matching, and (iii) frame-to-frame particle linking and corresponding velocity estimation. In this work, two validation approaches are employed to estimate the uncertainty and bias of the reconstructed 3D particle trajectories and velocities.

4.1. Static validation

The first approach comprises 'a static validation' and mainly tests the 3D particle position uncertainty resulting from camera calibration (internal and external camera parameters). Herewith, the maximum achievable accuracy of the reconstructed particle positions equals the residual error of the calibration (section 3.3). For this static validation, the 3D-PTV technique is applied to a fixed pattern with known geometry that is placed within the observation volume. The distance between the reconstructed target positions and their real (known) positions can then be used to derive the spatial distribution of the error made by the 3D-PTV reconstruction procedure. The same multiplane calibration unit as described in section 3.3 (camera calibration) is used as validation object because of its high positional accuracy. Similarly as during the calibration, the pattern-engraved aluminum plate is positioned at different elevations above the bed to acquire validation data throughout the entire volume. This static validation is done prior and independently from the measurements described in section 5, and comprises 13 vertical positions of the target plate with an intermediate vertical distance of 2 mm. The images taken at the odd positions are used for calibration (section 3.3), while the remaining eight other planes serve as validation data. Furthermore, the above-mentioned validation approach is employed to test the influence of the number of multiplane calibration planes, i.e. the density of calibration points in z-direction, by employing either one, three or five planes distributed over the water depth for calibration.

The side-by-side boxplots in figure 2 present the distribution of the distances $|x_i|$ between the known and the reconstructed $25 \times 14 \times 8$ validation points in the x-, y- and z-direction. In each boxplot (standard Tukey boxplot presented by Tukey (1977)), the central rectangle spans the first quartile to the third quartile of the errors $|x_i|$ (the interquartile range or IQR). The green bars indicate the median error of the reconstructed target positions, while the whiskers at the top and bottom mark the highest and lowest error of the validation points within 1.5 IQR of the upper and lower quartile, respectively. Although not shown in this paper, the errors increase near the edges of the calibration plate as could be expected from the least-squares calibration optimization. Figure 2 indicates that increasing the density of calibration points improves the overall calibration result, although the maximum deviations in the x- and y-direction are even with three calibration planes below the estimated accuracy of particle localization (0.09 mm). The superior accuracy obtained in the horizontal direction (x and y) compared to the vertical direction (z) is also expected given the higher spatial resolution in the horizontal plane resulting from the current (vertical) camera orientation.

4.2. Dynamic validation

The second and dynamic validation applied in this work is intended to test the other error sources related to 3D-PTV, namely particle identification and velocity quantification by tracking particles in time. The methodology of the adopted dynamic validation approach is inspired by the so-called 'dumbbell calibration technique' (Gülan *et al* 2012). Similar to Akutina (2015), two seeding particles (polystyrene microspheres with a particle diameter $d_p = 212 - 250$ μm) are glued onto the flat, black-coated end of a thin and handheld rod. The dumbbell rod is moved with a similar velocity as the particles during the measurements and recorded using the same experimental configuration (lighting, recording characteristics and camera configuration, …). The dumbbell recordings (20 s in total: 3000 dumbbell positions) are then processed using the same steps as used for the actual experiment: pre-processing to improve image contrast, particle localization using a Gaussian locator, correspondence matching through the epipolar line intersection technique, tracking particles throughout the image sequence, and finally the calculation of particle velocities by smoothing the trajectories with a Savitzky–Golay filter. A first assessment of the particle position accuracy is done by comparing the fixed dumbbell spacing $d = 8.98$ mm with the distance between the tracked particles at every time step (d_{track}):

$$\Delta d = d_{\text{track}} - d. \tag{4}$$

Figure 3 shows the distribution of the position error Δd over the entire validation measurement time (20 s), which suggests no significant bias towards larger or smaller values of the estimated distance. The average value of $|\Delta d|$ and the standard deviation of Δd equal 0.011 mm and 0.014 mm, respectively, which is an order of magnitude less than the particle size and thus assumed to be more than acceptable.

A direct assessment of the uncertainty of the particle velocities is made by expressing that the dumbbell particles should not move away or towards each other. Mathematically,

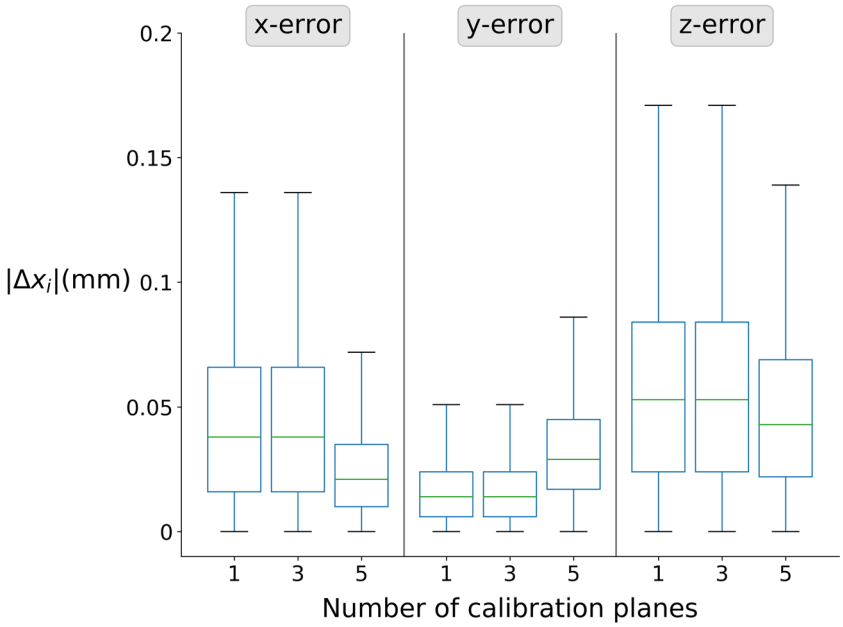

Figure 2. Comparison of the calibration errors for a varying number of calibration planes.

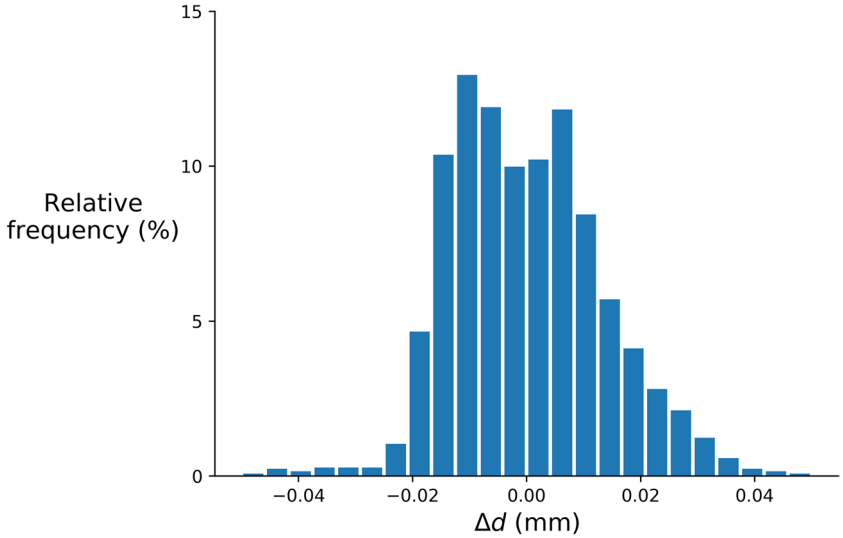

Figure 3. Relative distribution of the position error Δd during the dynamic dumbbell validation, depicting the frequencies of observations during the entire validation measurement time.

the velocity of dumbbell point 1 (with velocity $\boldsymbol{u_1}$) relative to dumbbell point 2 (with velocity $\boldsymbol{u_2}$) is computed by projecting their relative velocity $\boldsymbol{u_1} - \boldsymbol{u_2}$ onto the vector connecting the two particles $\boldsymbol{l}$, which results in the scalar $u_{1,2}$:

$$u_{1,2} = \frac{(\boldsymbol{u_1} - \boldsymbol{u_2}) \cdot \boldsymbol{l}}{|\boldsymbol{l}|}. \tag{5}$$

Since the particles are attached to a solid body and thus are unable to move toward or away from each other, the deviation of $u_{1,2}$ from zero (denoted as Δu) may be used as an indication of the velocity error during the experiment. The relative distribution of Δu over the entire calibration period is shown in figure 4, for which the average value of $|\Delta u|$ equals 0.89 mm s^{-1} and the standard deviation of Δu equals 1.32 mm s^{-1}. The average velocity of the dumbbell points, which is representative for the average velocity of the particles during the experiment, equals 51 mm s^{-1} over the entire 20 s validation period. This results in a relative error of the estimated velocities in the order of 2%, which in this paper is assumed to be acceptable.

Multiplying the dumbbell position error Δd (mean $|\Delta d| = 0.011$ mm; standard deviation $\Delta d = 0.014$ mm) with the camera frame rate (150 Hz), the velocity error estimated with Δu is reduced by almost a factor of 2. This confirms earlier findings (not shown in this paper) obtained through static validation that showed that the position errors have a certain bias depending on the region within the observation volume. This explains why the relative position error between points that are close together is smaller than the absolute position

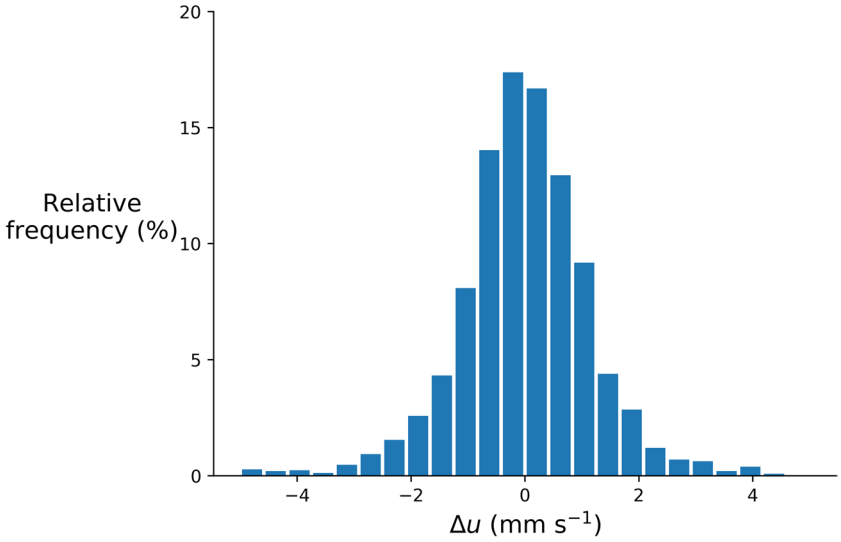

Figure 4. Relative distribution of the velocity error Δu during the dynamic dumbbell validation, depicting the frequencies of observations during the entire validation measurement time.

error (static validation) in some regions of the calibrated volume. The latter is beneficial for velocity estimations based on small particle displacements and improves the expected accuracy of the 3D velocity fields.

5. Results

5.1. Time-averaged embayment flow

Figure 5 presents the time- and depth-averaged streamlines and contours of the velocity magnitude $\sqrt{u^2+v^2}/U_\mathrm{b}$ in the cavity and adjacent main channel region, in which U_b denotes the bulk velocity in the main channel and u and v are the time- and depth-averaged velocity components in the x- and y-direction, respectively. Within the cavity, the depth-averaged flow field is characterized by a single recirculation cell or 'main gyre' that occupies almost the whole cavity area. As confirmed by the literature (Akutina 2015, Mignot *et al* 2019), the gyre has an ellipsoidal low-velocity core of which the main axes are approximately in line with the two horizontal diagonals of the square cavity. It is surrounded by a high-velocity (average velocity $0.2-0.3\ U_\mathrm{b}$) perimeter region that approximately follows the cavity walls. Additionally, small secondary cells with opposite sense of rotation (compared to the main gyre) are present in the corners of the cavity and at the leading (upstream) edge of the cavity adjacent to the main flow.

Exploiting the 3D-aspect of the 3D-PTV technique, figure 6 shows the time-averaged transverse velocities v (component normal to the geometrical interface between the main channel and the cavity) in the vertical plane of the interface ($y/W=0$). Although the exchange flow is highly dependent on the depth and longitudinal position along the interface, the flow mainly enters the cavity (red) in the downstream part and leaves the cavity (blue) in the upstream part. Moreover, the inflow in the downstream part seems most pronounced at the

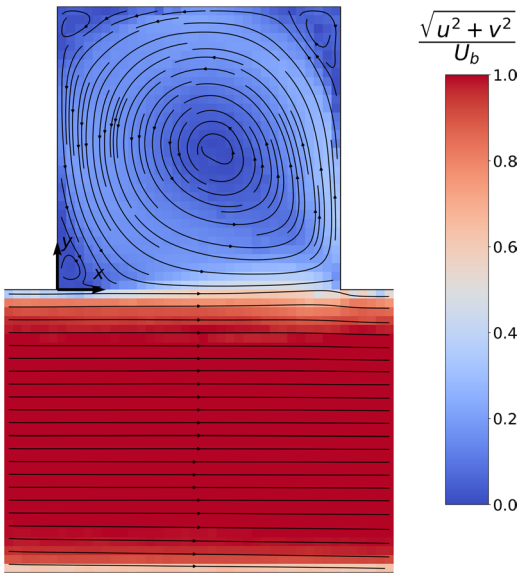

Figure 5. Time- and depth-averaged velocity field (contour plot and streamlines) in the cavity and main channel. The adopted coordinate system is indicated with origin at the upstream corner of the cavity.

bed, while the outflow in the upstream part appears more uniform over the entire water depth (in contrast with the literature stating that the outflow is concentrated near the surface). An interesting feature is the concentrated outflow (blue) near the downstream wall ($x/L=1$), which matches the findings of Akutina (2015). There, it was shown that this impression of local outflow is caused by a time-averaged shear layer deflection along the opening of the cavity, such that the shear layer's centerline impinges the downstream wall slightly inwards ($y/W>0$) from the cavity corner. However, just upstream of the downstream wall, part of the fluid (or particles for that matter) that has been deflected towards the embayment gets ejected back into the main flow, causing the impression of outflow with negative (blue) transverse velocities.

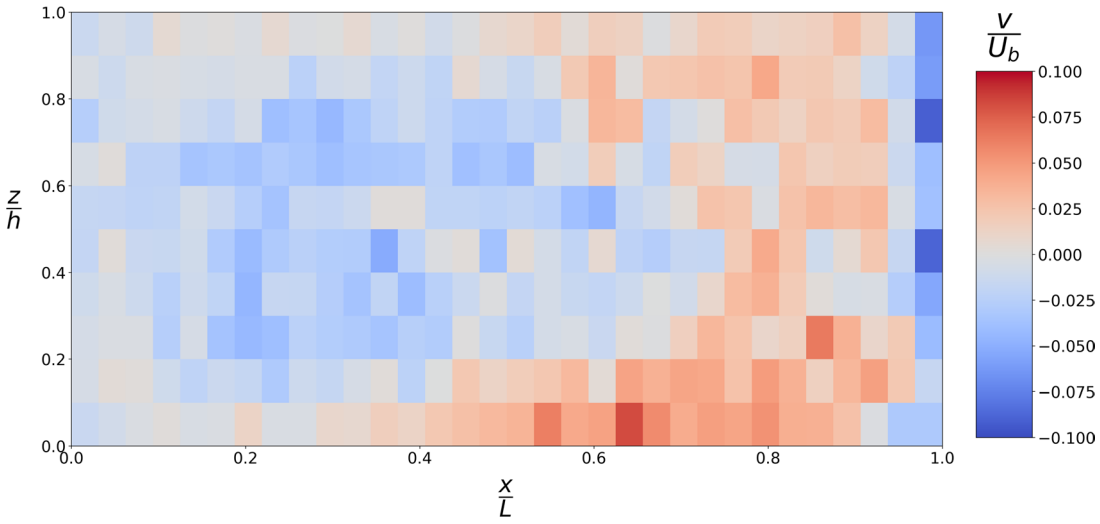

Figure 6. Time-averaged contour plot of the transverse velocity component v normal to the main channel-cavity interface at $y/W = 0$ (at the geometrical interface), in which blue colors corresponds to outflow out of the cavity and red colors corresponds to inflow into the cavity.

5.2. Eulerian mass exchange analysis

As mentioned in the introduction, the exchange between the main channel and the cavity is often parameterized using the mass exchange coefficient k, which can experimentally be quantified using the 'transverse velocity method'. Following Weitbrecht *et al* (2008), we first compute the instantaneous exchange velocity $E(z,t)$ by averaging the transverse velocity magnitude over the length of the main channel-cavity interface:

$$E(z,t) = \frac{1}{2L}\int_0^L |v(x,z,t)|\,\mathrm{d}x \tag{6}$$

where $v(x, z, t)$ is the transverse (cross-stream) velocity component at longitudinal position x and depth z in the vertical cross-section of the interface (figure 6), L equals the length of the cavity opening and the factor ½ originates from the fact that both the in- and outflow (positive and negative velocities) are summed in the integral of equation (6).

The mass exchange coefficient k is then calculated by normalizing the time-averaged value $\overline{E(z,t)}$ with the main stream velocity U_b to give

$$k(z) = \frac{\overline{E(z,t)}}{U_\mathrm{b}}. \tag{7}$$

Note that in the literature 3D velocity information is usually not available, such that the mass exchange coefficient is often determined at a single elevation z/h. We acknowledge that for river management purposes, the vertical profile of $k(z)$ seems less important, since usually computationally inexpensive 1D water quality models are employed which only require a single exchange parameter k. Therefore, albeit useful for research purposes, the vertical profile $k(z)$ is in this work further depth-averaged to derive a single parameter k_mean.

Starting from the Lagrangian 3D-PTV trajectories, computing the Eulerian transverse velocities v at the interface can be done using one of the two following methodologies. The first approach, referred to as '3D binning', averages the velocities of all particles located in 3D bins (voxels) near the interface, for which in this work the bin size equals $\Delta x_\mathrm{bin}/L = 0.03$, $\Delta y_\mathrm{bin}/W = 0.02$, $\Delta z_\mathrm{bin}/h = 0.1$ in the x-, y- and z-direction, respectively. For the bin direction perpendicular to the interface (y-direction), the bins start at $y/W = 0$ and end inside the cavity with the same bin size ($\Delta y_\mathrm{bin}/W = 0.02$) as Akutina (2015), for comparison purposes. In the second approach, referred to as '2D binning', all particles crossing a vertical intersection plane are included, for which in this work both the geometrical interface ($y/W = 0$) and the center of the 3D bins ($y/W = 0.01$) are selected. The velocities perpendicular to the vertical plane are then interpolated within 2D bins in the x- and z-direction with the same bin dimensions $\Delta x_\mathrm{bin}/L = 0.03$ and $\Delta z_\mathrm{bin}/h = 0.1$ as used with 3D binning.

Figure 7 gives $k(z)$ as a function of z/h using the two different binning approaches, which confirms that the exchange intensity varies significantly with depth (similar to figure 6). For this reason, obtaining a representative value for the depth-averaged exchange by quantifying k at a single elevation (as is often done in the literature) is less reliable than employing the 3D information of 3D-PTV to estimate k_mean. Nevertheless, evaluation of $k(z)$ at, for example, mid-depth for the profiles of figure 7 would yield a value (0.048, 0.072 and 0.078) which is close to the k_mean value (0.042, 0.067 and 0.074).

While the different profiles of figure 7 have a similar shape, suggesting that the mass exchange is stronger at intermediate depths, their depth-averaged values k_mean differ significantly. This difference is most probably caused by the fluctuating transverse velocities in the region of the interface, resulting in alternating positive and negative velocities v within the width of the 3D bins and/or at the location of the 2D binning planes. More specifically, fluctuations of a single trajectory add more than once to the bin-averaged values, of which the exact contribution depends on the number of appearances in every bin. Since the latter is strongly influenced by the choice of binning strategy, the shape and depth-averaged value of $k(z)$ are

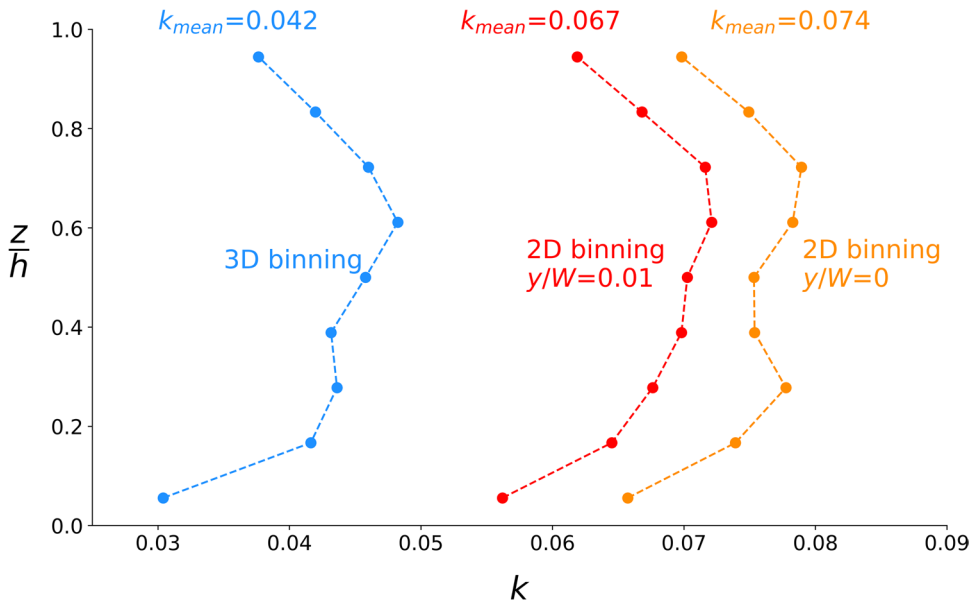

Figure 7. Vertical profiles of the mass exchange coefficient $k\,(z)$ and depth-averaged values k_{mean} using the 3D binning strategy (blue) or 2D binning strategy at $y/W = 0$ (orange) and $y/W = 0.01$ (red).

variable for the different binning approaches (2D versus 3D) and the corresponding size and location of the 2D or 3D bins. The latter seems confirmed by comparing the results of the 2D binning profiles of figure 7, in which a small shift towards the cavity ($y/W = 0 \rightarrow 0.01$) has a non-negligible influence on $k\,(z)$. To avoid the ambiguities related to the unsteady behavior of the flow and particle behavior near the geometrical interface, section 5.3 will present a novel, Lagrangian methodology to estimate a more reliable mass exchange coefficient.

In the literature, both Tuna *et al* (2013) and Akutina (2015) present a vertical distribution of $k\,(z)$ for similar Froude numbers, which also suggested that the mass exchange through the interface is stronger at intermediate elevations. Moreover, the '3D binning' results compare well with the 3D-PTV results of Akutina (2015), who used the same binning strategy and found a value of k_{mean} equal to 0.036 and 0.052 for $\text{Fr} = 0.29$ and $\text{Fr} = 0.32$, respectively. The lower k values of Tuna *et al* (2013), with $k_{\text{mean}} \cong 0.03$ for $\text{Fr} = 0.39$, might be explained by their higher Reynolds number and lower non-dimensional water depth h/L. Since Mignot *et al* (2017) showed that k increases as Re decreases and h/L increases, the relatively low Reynolds number and large h/L of the current experiment seem to explain a higher value of k.

However, since the main objective of this paper is to demonstrate the potential and added value of our new Lagrangian methodology to quantify the net mass exchange, no further attempt to reproduce flow conditions of the literature will be made in this paper. This will be the subject of future research on a larger scale setup, which will enable a more extensive comparison of the Eulerian k values with the literature.

5.3. Lagrangian mass exchange analysis

5.3.1. Description of the Lagrangian classification methodology. The relatively large variation of the Eulerian k values found in this work and reported in the literature suggests that the transverse velocity method might be a suboptimal methodology to compute a representative indicator for the intensity of net exchange. Indeed, the arbitrary choice of the transverse cross-section at which the transverse velocity components are integrated (i.e. the geometrical interface at $y/W = 0$) neglects the shear layer deflection towards the embayment and accompanying ejection at the downstream corner (figure 6). Moreover, earlier studies (e.g. Tuna *et al* 2013, Mignot *et al* 2016) showed that the shear layer centerline undulates significantly in time, such that the hydrodynamic interface between the main channel and the embayment seems a time-dependent and 3D curved surface. The fluctuating shear surface indicates that employing the geometrical interface $y/W = 0$ as a fixed boundary to evaluate in- or outflow might not be representative for the actual exchange. Moreover, even if the hydrodynamic interface between the main channel and the cavity could be determined unambiguously, multiple crossings of a single trajectory should not contribute multiple times to the quantification of the exchange velocity E (equation (6)) as explained in section 5.2.

Therefore, this work uses a Lagrangian approach by employing the 3D tracking capabilities of the 3D-PTV technique. By Lagrangian tracking of individual particles, it is possible to distinguish particles entering or leaving the cavity (exchange) and particles that only 'zigzag' across the geometrical interface (no exchange).

First, we define four vertical control sections as depicted in figure 8:

1. A transverse control section M_{us} in the upstream part of the main channel.
2. A transverse control section M_{ds} in the downstream part of the main channel.
3. A longitudinal control section I_{exch} inside the cavity.
4. The geometrical longitudinal interface I_{geom} between the main channel and the cavity.

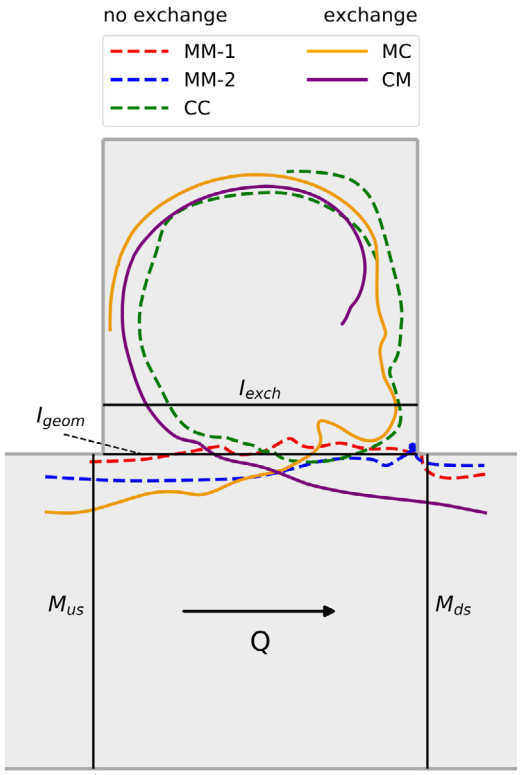

Figure 8. Schematic of the investigated flow domain (top view), with the four different control sections indicated. For each trajectory class, an illustrative example of an actually measured particle trajectory is depicted.

We then select the particles that traverse the interface I_{geom}, and thus are possible candidates for actual exchange. The selected particle trajectories are further analyzed by assessing how much and which control sections they intersect, in which particles crossing less than 2 times either M_{us}, M_{ds} or I_{exch} are labeled 'Lost'. The remaining particles can then be classified in four main classes as summarized in table 1, in which for each class the intersected control sections are marked by an X. For the class 'Lost', the trajectory length is too short to determine whether a particle has been entrained in the recirculation cell of the cavity, such that the particle trajectory cannot be included in the further Lagrangian analysis. Figure 8 motivates that particles that are classified as CC should cross I_{exch} twice (hence 2X in table 1), one time before and one time after they intersect with I_{geom}. All particles that belong to class MM or CC traverse the geometrical interface I_{geom} but, respectively, do not enter or leave the recirculation cell inside the cavity.

A visual analysis of the trajectories classified in MM shows that two physical processes cause their paths to intersect the geometrical interface:

1. MM-1: Particles oscillate back and forth across the interface when traveling downstream ('zigzagging') as a result of their entrainment in the advected shear layer vortices, which are characterized by such transverse velocity fluctuations.
2. MM-2: Particles trajectories are deflected towards the embayment due to the shear layer deflection (see section 5.2), but finally 'escape' the cavity and are ejected back into the main stream just upstream of the downstream wall.

Table 1. Classification of particle trajectories based on vertical control sections.

Class	I_{geom}	M_{us}	M_{ds}	I_{exch}	Net exchange?
Lost	X	One out of three			Unknown
MM: main–main	X	X	X		No exchange
CC: cavity–cavity	X			2X	No exchange
MC: main–cavity	X	X		X	Exchange
CM: cavity–main	X		X	X	Exchange

An illustrative example of these two types of trajectories belonging to MM, as well as examples of the other three classes, is graphically shown in figure 8. It seems evident that only particles of class MC or CM add to the net exchange.

5.3.2. Definition of the control sections. The suggested classification is mainly determined by a well-chosen location of the control sections M_{us}, M_{ds} and I_{exch}. However, since it can be assumed that particles within the main channel do not travel in the upstream direction, the exact location of M_{us} and M_{ds} herein is of minor importance as long as the immediate surroundings of the cavity corners are excluded. In this work, M_{us} is chosen at $x/L = -0.025$ and M_{ds} at $x/L = 1.025$. On the other hand, the transverse cross-section y/W of plane I_{exch} should be chosen with great care to guarantee that the particles of class MC or class CM are actually entrained in the cavity or main flow, respectively. To this end, one could argue that choosing I_{exch} in the middle of the cavity ($y/W = 0.5$) seems a safe solution. However, defining I_{exch} further away from the cavity opening (I_{geom}) increases the probability that a tracked particle becomes 'lost' during tracking from M_{us} to I_{exch} or from I_{exch} to M_{ds}, making it impossible to assign it to one of the four main trajectory classes.

Therefore, the location of I_{exch} is chosen as close as possible to the cavity opening ($y/W = 0$), while ensuring that 'zigzagging' or 'ejected' particle trajectories are excluded. Since it can be assumed that the inertia of the particles is negligible (Stokes number $\text{St} = 0.04 < 0.1$), the maximum penetrating distance y/W of 'ejected particles' is estimated based on the hydrodynamic processes governing the trajectories of MM-1 and MM-2. For MM-1, half of the (maximum) mixing layer width seems a good estimation, while for MM-2, the extent of local outflow near the downstream corner is estimated by the sign of the local transverse velocity components v.

For the current experiment, the estimated shear layer width grows from $\delta/L = 0.07$ to a maximum $\delta/L = 0.23$ (similar to the results of Mignot *et al* 2017), while negative transverse velocities (outflow) near the downstream wall disappeared for $y/W > 0.05$ (similar to the results of Akutina 2015). Using half of the mixing layer width as the most stringent criterion

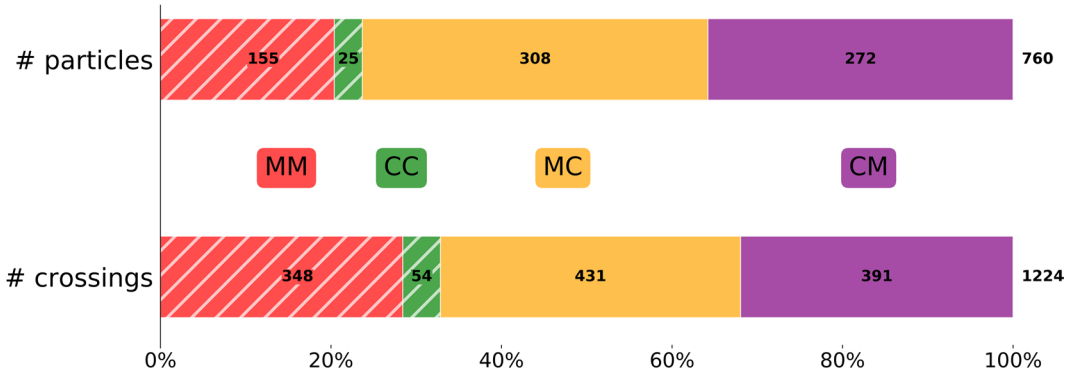

Figure 9. Class distribution of the particle trajectories, in which for each class the total number of particles (first row) or crossings with I_{geom} (second row) is displayed in the corresponding bar.

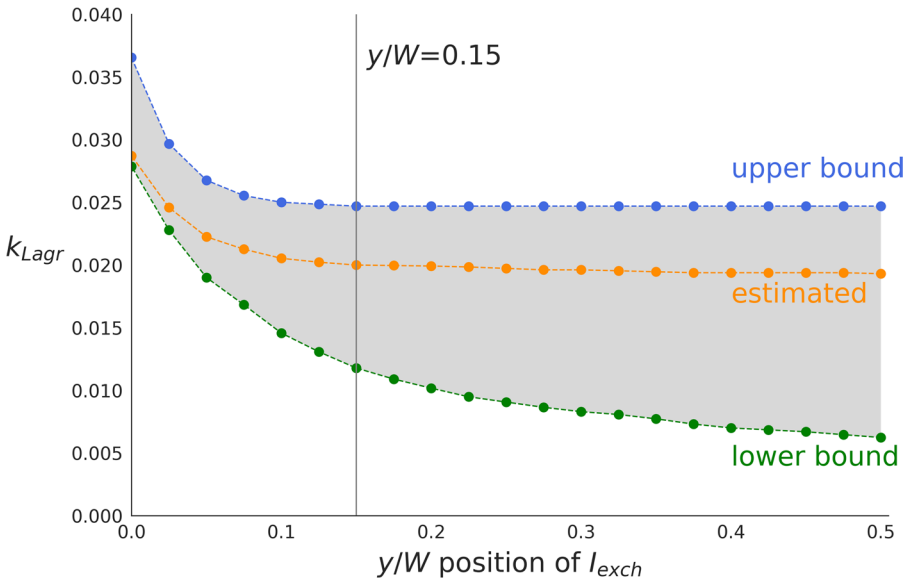

Figure 10. The Lagrangian mass exchange coefficient k_{Lagr} for different positions of I_{exch}, in which the best estimate is indicated in orange and the lower and upper bound are displayed in green and blue respectively. The gray area represents the uncertainty due to particle loss.

and adding an additional safety for possible shear layer undulation, the location of I_{exch} is set at $y/W = 0.15$. Visual analysis of the classified trajectories confirmed that this choice of I_{exch} is sufficient to avoid that particles still escape after crossing I_{exch}. Moreover, the results that will be presented in section 5.3.4 suggest that if I_{exch} is not located too close to the geometrical interface, the exact location of I_{exch} has only a minor influence on the Lagrangian mass exchange coefficient which will be explained hereafter.

5.3.3. Description of the Lagrangian mass exchange coefficient. One could argue that a more reliable definition of the mass exchange coefficient k would be to compute the exchange velocity E (equation (6)) by only integrating the transverse velocities of class MC and CM. However, these particles only enter or leave the cavity occasionally and are often characterized by a higher transverse velocity compared to other particles that are transported through the interface. Therefore, quantifying E solely based on the relatively high transverse velocities of MC and CM seems not representative for the time-averaged exchange flow. Moreover, even with this trajectory-based selection of the transverse velocities at the interface, multiple crossings of the trajectories of MC and CM remain included with the aforementioned methodology, as explained in section 5.2. To solve these complications, this paper presents a Lagrangian alternative to determine the mass exchange coefficient.

In analogy with the classical expression for k ($= E/U_b$), we define the (Lagrangian) mass exchange coefficient as the ratio between the mass exchanged between the cavity and main channel ($\sim E$) and the mass supplied in the main channel from upstream ($\sim U_b$). In practice, our so-called k_{Lagr} is estimated by classifying (counting) the 3D-PTV measured particles based on the presented classification methodology of section 5.3.1.

Following the Eulerian definition of the exchange velocity E (equation (6)), the mass being exchanged could be determined by counting all particles that cross I_{geom}. However, as explained in section 5.3.1, only the particles that belong to class MC and CM add to the net exchange, of which in this work only the particles in class MC are adopted to quantify k_{Lagr}. This choice for a single particle class avoids that both the in- and outflow are included and matches methodologically to the factor ½ in equation (6).

For the mass supplied from upstream in the main channel, the amount of particles crossing M_{us} could seem a reasonable estimation. However, setting M_{us} as the sole selection criterion for the particles representing main channel supply would make the probability of losing particles during tracking much more likely for class MC compared to the particles crossing M_{us}. To make the stringency of the imposed requirements for both groups comparable, the particles supplied from the main channel are defined as the particles crossing both M_{us} and M_{ds}. If we assume that the probability of losing a particle during tracking is comparable between $M_{us} - M_{ds}$ and $M_{us} - I_{geom}$ (both regions located in the main channel), setting a start and end section for every group minimizes the possible bias due to a different fraction being lost.

As a result, the basic definition for our Lagrangian mass exchange coefficient k^0_{Lagr} becomes

$$k^0_{Lagr} = \frac{\text{Mass exchanged}}{\text{Mass supplied in the main channel}} = \frac{\#\text{MC}}{\#\text{Main}} \quad (8)$$

in which # denotes the amount of particles during the entire measurement period and 'Main' represents the particles crossing both M_{us} and M_{ds} in the main channel.

As will be specified in section 5.3.4, a significant part of the possible exchange candidates (particles crossing M_{us} and I_{geom}) could not be classified for the current dataset because they became 'Lost' before crossing either M_{ds} (MM) or I_{exch} (MC). Even though two crossing criteria (M_{us} and M_{ds}) were set to estimate #Main to equalize the stringency of the selection criteria these unclassified particles result in a possible underestimation of the numerator compared to the denominator of equation (8). For this reason, we introduce a correction factor in equation (8), which represents the hypothesized fraction of the non-classified particles crossing M_{us} and I_{geom} that would have crossed I_{exch} in case of no particle loss:

$$k_{Lagr} = \underbrace{\frac{\#\text{MC}}{\#\text{Main}}}_{\text{ideal dataset}} + \underbrace{\frac{\text{correction}}{\#\text{Main}}}_{\text{with loss of particles}}. \quad (9)$$

For 'the ideal dataset', no particles are lost and all particles crossing M_{us} and I_{geom} are either categorized in class MC or MM, yielding correction factor of zero, thus $k^0_{Lagr} = k_{Lagr}$. For actual experiments, however, loss of particles during tracking always occurs.

In this work, we estimate the net exchanged fraction of non-classified particles by selecting those trajectories for which the end position is located within the cavity area ($y > 0$) and the end velocity is directed towards the cavity ($v > 0$). Moreover, a lower and upper bound are determined to get a feel for the uncertainty on this best estimate (i.e. corrected k_{Lagr} defined by equation (9)). The lower bound for k_{Lagr} is found by setting the correction factor equal to zero, thus assuming that all non-classified trajectories crossing M_{us} and I_{geom} do not enter the cavity (MM). In contrast, considering that all non-classified particles will cross I_{exch}, and thus belong to MC, yields an upper bound for the correction factor and k_{Lagr}.

5.3.4. Lagrangian results. In this section, the relative distribution of the different trajectory classes and the corresponding mass exchange coefficient k_{Lagr} will be presented for the current experiment. However, in this first application of our 3D-PTV setup, the camera positions and seeding density were initially chosen to obtain a global view of the 3D flow in and around the cavity instead of acquiring long trajectories for the Lagrangian trajectory analysis. In this respect, a relatively large seeding density was used to accelerate the convergence of the time-averaged flow fields shown in figures 5 and 6. Moreover, the cameras were positioned to achieve a relatively large overlapping field of view (figure 1), such that the entire 3D flow field could be reconstructed without repositioning the cameras. Although the post-processing routines described in section 3 were optimized to enhance the tracking efficiency, a significant fraction of all particles that crossed I_{geom} became lost during tracking. Over the entire measurement period of 120 s, approximately 2600 tracked particles passed the geometrical interface I_{geom}, of which for our choice of I_{exch} ($y/W = 0.15$) 70% could not be assigned to one of the four main trajectory classes. Similarly, approximately 800 possible exchange candidates crossed M_{us} and I_{geom} (equation (8)), of which 40% became lost during tracking before intersecting with M_{ds} (MM) or I_{exch} (MC) for I_{exch} at $y/W = 0.15$.

The authors admit the potential bias caused by a possible different probability of loss depending on the particle trajectory, and do not claim statistical convergence of the following Lagrangian quantitative results (in contrast with the time-averaged velocity fields of figures 5 and 6). Nonetheless, since this work is mainly intended to illustrate the potential of the suggested Lagrangian research methodology, preliminary results are presented hereafter.

Firstly, figure 9 displays the distribution of the particles over the four main trajectory classes for I_{exch} at $y/W = 0.15$, in which for each class the total number of particles as well as the number of times the particles cross I_{geom} is displayed (one 'zigzag' counts for two crossings). The total number of particles/crossings over all four categories is indicated at the right hand side of each stacked bar graph. In spite of the significant fraction of particles that could not be classified, the relative fraction of particles belonging to class MM and CC (hatched area in figure 9) seems a first indication of the error made by the common Eulerian approach. Indeed, the Eulerian quantification of k integrates the transverse velocities of all particle trajectories crossing I_{geom}, even though the trajectory crossings of MM and CC do not add to the net exchange. Note that complementary to figure 9, the appendix of this work presents the particle class distribution for a range of y/W positions of I_{exch} to indicate the influence of the chosen position of I_{exch}.

Figure 10 gives for the current experiment the estimated k_{Lagr} (orange), as well as the lower bound (green) and upper bound (blue) in function of the chosen position of I_{exch} (y/W). Setting I_{exch} further inside the cavity (increasing y/W) strengthens the imposed requirements for MC and thus reduces the numerator of the first term in the right-hand side of equation (9), resulting in a decrease of k_{Lagr}. Nonetheless, it can be observed that the estimated k_{Lagr} remains almost constant for $y/W > 0.12$, being half of the suggested shear layer width $\delta_{max}/L = \delta_{max}/W = 0.23$. Therefore, our choice

for I_{exch} at $y/W = 0.15$ seems appropriate to select the net exchanging particles, which gives a value of 0.020, 0.012 and 0.025 for the best estimate, lower and upper bound of k_{Lagr}, respectively.

Not surprisingly, k_{Lagr} is less than half of the Eulerian k_{mean} values found in section 5.2, which confirms our statement that the common transverse velocity method significantly overestimates the intensity of mass exchange. Moreover, our Lagrangian methodology avoids that the quantification of mass exchange is based on an ambiguous definition of the transverse velocities at 'the interface'. Compared to the large variation of the Eulerian k_{mean} values depending on the integration plane and binning strategy (0.042–0.074), figure 10 shows that the only determining factor inherent to the Lagrangian methodology (i.e. the location of I_{exch}) has only little influence on the estimated k_{Lagr}.

We acknowledge the significant uncertainty on the estimated k_{Lagr} (upper–lower bound), which is indicated in gray in figure 10. Nonetheless, even the upper bound of k_{Lagr} is significantly smaller than the Eulerian k_{mean} values. Moreover, it can be assumed that fine-tuning the optical setup (camera arrangement) and seeding density of our 3D-PTV technique will facilitate the tracking for future experiments and reduce the amount of particles being lost. Finally, being applicable to even a suboptimal dataset, the results presented in this paper indicate the potential of the presented methodology.

6. Conclusion

This paper has presented the design, validation and application of a recent 3D-PTV setup, which was employed to study mass exchange in an open-channel flow past a lateral, square cavity using both an Eulerian and a Lagrangian research methodology. A multiplane 3D calibration technique and an advanced particle linking strategy were implemented to increase the accuracy and average length of the 3D particle trajectories. Both a static and dynamic experimental validation proved that the 3D-PTV setup allows for highly accurate 3D positions and velocities.

The resulting 3D flow velocities were then used to obtain a better understanding of the 3D distribution of the in- and outflow between the cavity and the main stream. Analysis of the flow velocities at the geometrical interface showed that inflow mainly occurs at the downstream end of the cavity opening, concentrated near the bed, while the particles tend to leave the cavity more uniformly over the water depth in the upstream part of the interface.

An Eulerian approach was then applied to determine the (velocity-based) mass exchange coefficient, which is a lumped parameter that is usually considered representative for the time-averaged exchange intensity. This analysis confirmed earlier observations in the literature that the mass exchange coefficient is highly dependent on depth. Hence, determining the mass exchange coefficient from the transverse velocities (measured or calculated) in the geometrical interface at a given depth (2D approach) does not necessarily lead to representative indicator for the (depth-averaged) exchange of fluid and mass with the lateral embayment.

But even with a 3D Eulerian approach, one should be aware that the geometrical interface may not be the most suitable boundary to evaluate in- or outflow between the cavity and the main stream. In reality, the shear layer centerline first deflects into the cavity and is then ejected back into the main flow just upstream of the downstream corner, while also being characterized by fluctuating transverse velocities arising from the shear layer vortices. As a consequence, not all particles traversing the geometrical interface really contribute to the net exchange between the cavity and the main stream.

Therefore, a Lagrangian analysis of the particle trajectories was explored, in which a novel classification system allowed to identify the oscillating particles that do not add to the net exchange. Moreover, we proposed an alternative, Lagrangian definition of the mass exchange coefficient that is not affected by errors related to the fluctuating character of the particle trajectories near the interface. Even though the measurement conditions of the current experiment (initially chosen to obtain a global view of the 3D flow field in and around the cavity) appeared suboptimal for this Lagrangian trajectory analysis, the results presented in this paper suggest that our Lagrangian methodology has a large potential to reliably study mass exchange. Note that the presented trajectory classification and Lagrangian mass exchange coefficient are not only applicable to passive particle exchange, but can also be used to study non-passive particle (i.e. sediment-like) transport.

Future work will concentrate on the refinement of the 3D-PTV setup (i.e. camera arrangement, seeding density, etc) to reduce the fraction of particles being lost during tracking, and as such reduce the uncertainty on the presented Lagrangian mass exchange results. Future experiments in a larger-scale setup will then be analyzed to present a more in-depth quantitative comparison between the common (Eulerian) and alternative (Lagrangian) methodologies to quantify the mass exchange.

Acknowledgments

The authors are grateful to Dr Emmanuel Mignot of INSA Lyon for stimulating discussions during this work, and to the anonymous reviewers for their helpful comments which significantly improved the quality of this paper. The first author is a PhD fellow of the Special Research Fund (BOF) of Ghent University.

Appendix. Particle class distribution in function of y/W position of I_{exch}

Complementary to figure 9 (I_{exch} at $y/W = 0.15$), this appendix presents the class distribution of the particle trajectories for different y-positions of I_{exch}. Figure A1 presents the total number (indicated as #) of particles of each trajectory class in function of the y/W position of I_{exch}, while figure A2 gives the corresponding number of crossings with I_{geom}. Similarly as what was stated regarding figure 10, setting I_{exch} further inside the cavity (increasing y/W) strengthens the imposed requirements

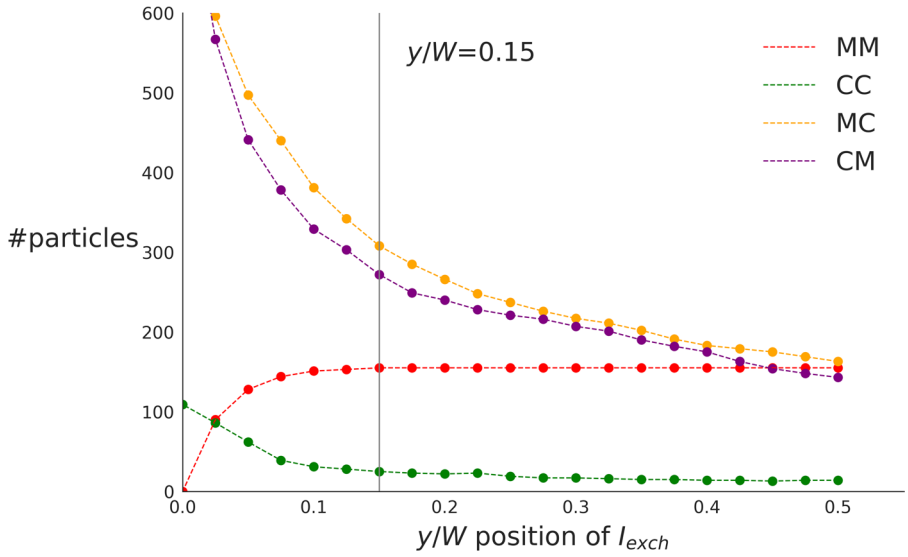

Figure A1. Class distribution of the particle trajectories, in which for each class the total number of particles is displayed in function of the chosen y/W position of I_{exch}.

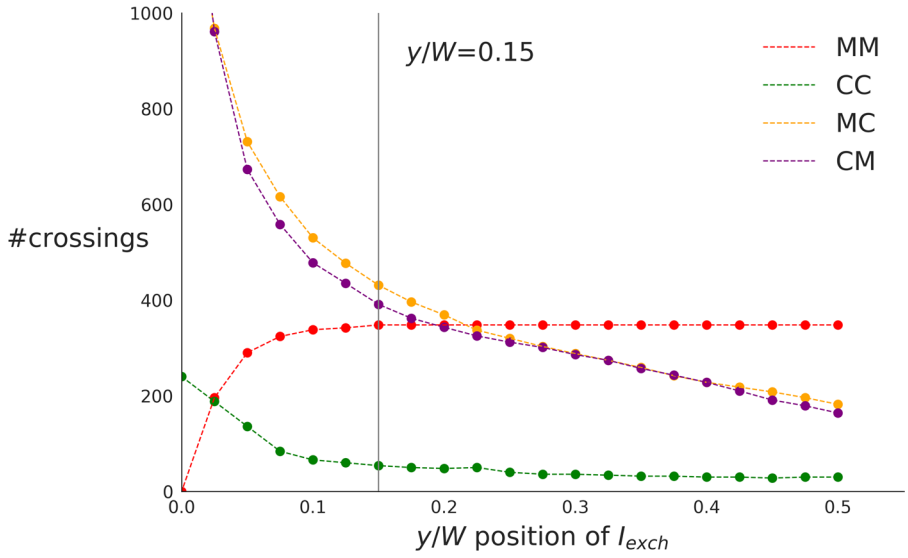

Figure A2. Class distribution of the particle trajectories, in which for each class the total number of crossings with I_{geom} is displayed in function of the chosen y/W position of I_{exch}.

for MC, CM and CC which reduces the amount of particles that were assigned to that class. In contrast, setting the location of I_{exch} at higher y/W reduces the stringency of the criterion for class MM which explains the increasing trend of the MM class. Especially for class MC and MC, the position of I_{exch} appears to have a non-negligible effect on the amount of particles categorized to that class. However, since for increasing y/W also the total number of particles that could be classified (sum of all classes) is reduced, the decreasing number of particles of class MC and CM is almost certainly caused by an increase loss of particles during tracking. Moreover, it can be observed that the amount of particles and crossings of classes MM and CC (the zigzagging particle trajectories) remain almost constant for $y/W > 0.12$ (estimated extent of the mixing layer). Therefore, the chosen position $y/W = 0.15$ used in this work seems an appropriate choice to distinguish the net exchange reliably.

Note that for future experiments, the optical setup (camera arrangement) and seeding density of the 3D-PTV technique will be fine-tuned to facilitate the measurement of long trajectories and reduce the loss of particles during tracking. In that case, it can be assumed that the decreasing trend of class MC and CM with increasing y/W will be mitigated, such that the sensitivity of the presented Lagrangian class distribution to the location of I_{exch} will be reduced.

ORCID iDs

L Engelen https://orcid.org/0000-0003-1013-2181
T De Mulder https://orcid.org/0000-0003-0823-105X

References

Adrian R J and Westerweel J 2011 *Particle Image Velocimetry* vol 30 (Cambridge: Cambridge University Press)

Akutina Y 2015 Experimental investigation of flow structures in a shallow embayment using 3D-PTV *PhD Thesis* McGill University

Akutina Y, Mydlarski L, Gaskin S and Eiff O 2018 Error analysis of 3D-PTV through unsteady interfaces *Exp. Fluids* **59** 53

Bradski G 2000 The OpenCV Library *Dr. Dobb's Journal of Software Tools*

Constantinescu G, Sukhodolov A and McCoy A 2009 Mass exchange in a shallow channel flow with a series of groynes: LES study and comparison with laboratory and field experiments *Environ. Fluid Mech.* **9** 587

Dracos T (ed) 2013 *Three-Dimensional Velocity and Vorticity Measuring and Image Analysis Techniques: Lecture Notes from the Short Course* (*Zürich, Switzerland*, *3–6 September 1996)* vol 4 (Berlin: Springer)

Jamieson E and Gaskin S 2007 Laboratory study of 3-dimensional characteristics of recirculating flow in a river embayment *Proc. XXXII IAHR Congress (Venice, Italy – 2007)*

Gülan U, Lüthi B, Holzner M, Liberzon A, Tsinober A and Kinzelbach W 2012 Experimental study of aortic flow in the ascending aorta via particle tracking velocimetry *Exp. Fluids* **53** 1469–85

Hays J R 1966 Mass transport mechanisms in open-channel flow *PhD Thesis* Vanderbilt University

Hinterberger C, Fröhlich J and Rodi W 2007 Three-dimensional and depth-averaged large-eddy simulations of some shallow water flows *J. Hydraul. Eng.* **133** 857–72

Kieft R, Schreel K, van der Plas G and Rindt C 2002 The application of a 3D PTV algorithm to a mixed convection flow *Exp. Fluids* **33** 603–11

Kreizer M and Liberzon A 2011 Three-dimensional particle tracking method using FPGA-based real-time image processing and four-view image splitter *Exp. Fluids* **50** 613–20

Maas H G, Gruen A and Papantoniou D 1993 Particle tracking velocimetry in three-dimensional flows *Exp. Fluids* **15** 133–46

Marxen M, Sullivan P E, Loewen M R and Jähne B 2000 Comparison of Gaussian particle center estimators and the achievable measurement density for particle tracking velocimetry *Exp. Fluids* **29** 145–53

Meller Y and Liberzon A 2016 Particle data management software for 3d particle tracking velocimetry and related applications–the flowtracks package *J. Open Res. Softw.* **4**

Mignot E, Cai W, Launay G, Riviere N and Escauriaza C 2016 Coherent turbulent structures at the mixing-interface of a square open-channel lateral cavity *Phys. Fluids* **28** 045104

Mignot E, Cai W, Polanco J I, Escauriaza C and Riviere N 2017 Measurement of mass exchange processes and coefficients in a simplified open-channel lateral cavity connected to a main stream *Environ. Fluid Mech.* **17** 429–48

Mignot E, Cai W and Riviere N 2019 Analysis of the transitions between flow patterns in open-channel lateral cavities with increasing aspect ratio *Environ. Fluid Mech.* **19** 231–53

OpenPTV Consortium 2013 Open Source Particle Tracking Velocimetry (http://www.openptv.net/)

Mizumura K and Yamasaka M 2002 Flow in open-channel embayments *J. Hydraul. Eng.* **128** 1098–101

Raffel M, Willert C E, Scarano F, Kähler C J, Wereley S T and Kompenhans J 2018 *Particle Image Velocimetry: a Practical Guide* (Berlin: Springer)

Schindelin J *et al* 2012 Fiji: an open-source platform for biological-image analysis *Nat. Methods* **9** 676

Taylor G I 1935 Statistical theory of turbulence. IV. Diffusion in a turbulent air stream *Proc. R. Soc.* A **151** 465–78

Taylor G I 1954 The dispersion of matter in turbulent flow through a pipe *Proc. R. Soc.* A **223** 446–68

Tropea C, Yarin A L and Foss J F E 2007 *Springer Handbook of Experimental Fluid Mechanics* (Berlin: Springer)

Tukey J W 1977 *Exploratory Data Analysis* (Reading, MA: Addison-Wesley)

Tuna B A, Tinar E and Rockwell D 2013 Shallow flow past a cavity: globally coupled oscillations as a function of depth *Exp. Fluids* **54** 1586

Uijttewaal W S J, Lehmann D V and Mazijk A V 2001 Exchange processes between a river and its groyne fields: model experiments *J. Hydraul. Eng.* **127** 928–36

Valentine E M and Wood I R 1979 Experiments in longitudinal dispersion with dead zones *ASCE J. Hydraul. Div.* **105** 999–1016

Walpot R J E, Rosielle P C J N and van der Geld C W M 2006 Design of a set-up for high-accuracy 3D PTV measurements in turbulent pipe flow *Meas. Sci. Technol.* **17** 3015

Weitbrecht V, Socolofsky S A and Jirka G H 2008 Experiments on mass exchange between groin fields and main stream in rivers *J. Hydraul. Eng.* **134** 173–83

Willneff J 2003 A spatio-temporal matching algorithm for 3D particle tracking velocimetry *PhD Thesis* ETH Zürich

Xu H 2008 Tracking Lagrangian trajectories in position–velocity space *Meas. Sci. Technol.* **19** 075105

Xu H and Bodenschatz E 2008 Motion of inertial particles with size larger than Kolmogorov scale in turbulent flows *Physica* D **237** 2095–100